Earth **Surface**
Dynamics
Discussions

Optimization of passive acoustic bedload monitoring in rivers by signal inversion

Mohamad Nasr[1], Adele Johannot[1], Thomas Geay[2,3], Sebastien Zanker[4], Jules Le Guern[,3], Alain Recking[1]

[1]University Grenoble Alpes, INRAE, ETNA, Grenoble, France.
5   [2] Office National des Forêts, service Restauration Terrain Montagne 38000 Grenoble, France.
[3] GINGER BURGEAP, R&D, 38000 Grenoble, France.
[4]EDF Hydro, DTG, 38950 Saint-Martin-le-Vinoux, France.

Correspondence to: Mohamad Nasr (mohamadnasr94@gmail.com)

Abstract.

10   Recent studies have shown that hydrophone sensors can monitor bedload flux in rivers by measuring the self-generated noise (SGN) emitted by bedload particles when they impact the riverbed. However, experimental and theoretical studies have shown that the measured SGN depends not only on bedload flux intensity but also on the propagation environment, which differs between rivers. Moreover, the SGN can propagate far from the acoustic source and be well measured at distant river positions where no bedload transport exists. It has been shown that this dependence of the SGN measurements on the propagation

15   environment can significantly affect the performance of monitoring bedload flux by hydrophone techniques. In this article, we propose an inversion model to solve the problem of SGN propagation and integration effect. In this model, we assume that the riverbed acts as SGN source areas with intensity proportional to the local bedload flux. The inversion model locates the SGN sources and calculates their corresponding acoustic power by solving a system of linear algebraic equations accounting for the actual measured cross-sectional acoustic power (acoustic mapping) and attenuation properties. We tested the model using two

20   field campaigns conducted in 2018 and 2021 on the Giffre River in the French Alps, which measured the bedload SGN profile (acoustic mapping with a drift boat) and bedload flux profile (direct sampling with an Elwha sampler). Results confirm that the bedload flux profile better correlates with the inversed acoustic power than measured acoustic power. Moreover, it was possible to fit the two field campaign with a unique curve after inversion, which was not possible with the measured acoustic data. The inversion model shows the importance of considering the propagation effect when using the hydrophone technique

25   and offers new perspectives for the calibration of bedload flux with SGN in rivers.

1 Introduction

Bedload controls rivers' morphodynamics and can directly impact population safety, hydraulic structures' stability, and river ecological systems. But bedload is also a consequence of the morphology (Recking et al., 2016) as it occurs at different rates across the channel (Gomez, 1991) due to heterogeneity in riverbed grains size distribution (GSD), flow depth, and velocity

30   (Whiting and Dietrich, 1990; Ferguson et al., 2003). Understanding the transport dynamics thus requires coupling of water flow gradient, river bed adjustment, and roughness conditions (Ergenzinger et al., 1994). This explains why estimating bedload

transport and the bed response is not an easy task. For instance, computation with bedload equations usually considers the average shear stress τ, occulting the non-linear effect of variability within the section (Ferguson et al., 2003; Recking, 2013). On the other hand, direct monitoring of bedload transport (e.g., pressure difference samplers) is expensive and time-consuming

35 and does not permit high-resolution sampling (Claude et al., 2012).

Given these difficulties, particular interest has been given to indirect surrogate bedload monitoring using different sensors (Gray et al., 2010). These techniques permit high-resolution monitoring even under extreme flow conditions. One category of these techniques is the passive sensing technique, which measures the signals emitted by bedload impacts. Bedload particles can impact an object specifically designed for this measurement; for instance, geophones are used to measure the vibration

40 generated by particles' impacts on steel plates (Rickenmann et al., 2014), and microphones are used to measure the acoustic noise generated inside impacted steel pipes (Mao et al., 2016). Another approach consists in measuring directly the signal emitted when the transported grains hit the riverbed. For instance, seismometers measure ground vibration due to bedload impacts (Gimbert et al., 2019; Bakker et al., 2020), whereas hydrophones measure the bedload self-generated acoustic noise (SGN) (Johnson and Muir, 1969; Barton et al., 2010). This paper concerns this later technique.

45 Recent studies have shown that the measured SGN depends not only on bedload characteristics but also on the sound propagation properties of the river, which is controlled by multiple factors such as slope, water level, and bed roughness (Wren et al., 2015; Rigby et al., 2016; Geay et al., 2017). For example, in their attempt to derive a general calibration curve between bedload flux and acoustic power, Geay et al. (2020) observed that the spectral content of SGN was highly correlated to the river slope, suggesting a significant effect of local propagation. This dependence on the local conditions may have contributed

50 to the general scattering obtained between specific bedload flux and acoustic power in the mentioned work. On the other hand, this also suggests that accounting for propagation effects should improve the relationships between bedload and SGN characteristics. Besides, an inversion method that solves the issue of spectrum shape and estimates the entire bedload GSD curve has been proposed by Petrut et al. (2018). However, the inversion results overestimate sampled values for five gravel-bed (Geay et al., 2018), suggesting that the acoustic power measured in rivers may not adequately capture the finest materials

55 contained in bedload due to signal attenuation at high frequencies.

The correction of signal attenuation due to propagation can be achieved by using source inversion methods. The inversion method uses propagation laws to reconstruct the strengths and location of acoustic sources from the measured signal. It is extensively studied and used in acoustical engineering applications such as detecting noise sources for jet engines using a beamforming microphone array (Presezniak and Guillaume, 2010; Arthur et al., 2017; Madoliat et al., 2017). To our

60 knowledge, no studies have dealt with bedload SGN sources inversion in rivers, despite its evident interest for bedload monitoring, as the hydrophone measures distant bedload impacts in the river cross-section: inversion would give access to the characteristics of bedload SGN sources and improve our understanding of the bedload characteristics and distribution in the rivers. Recently, Geay et al. (2019) proposed a protocol to estimate the acoustic signal attenuation in rivers using a transmission loss function (TL) calibrated with an active acoustic experiment.

65 In this paper, we use this work for developing an inversion model that gives access to the SGN sources by correcting the attenuation of the measured SGN. First, we define the bedload SGN source and the transmission loss function in the river. Secondly, we present the inversion model adopted for SGN sources. Finally, we test the proposed model's performance in the field with two experiments: 1) an active test (in the river and the lab) using a known emitted signal, 2) a passive test using bedload SGN measurements where the inversed source are compared with bedload physical sampling.

2 Theoretical definitions

2.1 Bedload SGN source

Acoustic noise corresponds to minute impulsive pressure (μPa^2) fluctuations initiated at the source position and propagated in the river. By convention, the intensity of an acoustic source is defined as the intensity measured at a distance of 1 m from the source without being attenuated (Jensen et al., 2011). Multiple studies have examined the generation of acoustic noise by

75 impacting body in the air (Koss and Alfredson, 1973; Koss et al., 1974; Akay et al., 1978). However, less research was dedicated to studying the acoustic noise generated by underwater sediment impacts (Thorne and Foden, 1988; Thorne, 1990). The physical model proposed by Thorne and Foden (1988) suggests a frequency-based solution of sound generated due to a sphere-sphere impact underwater. This model shows that the energy spectrum e ($\mu Pa^2 \cdot s \cdot Hz^{-1}$) is dependent on multiple parameters such as particle size, impact velocity, sediment and water mechanical properties, and position of the recording

80 sensor with respect to the noise source.

Because the SGN noise corresponds to continuous random impulses in the river (Geay, 2013), bedload SGN sources cannot be considered scattered point impacts. Instead, bedload SGN sources are here defined as separate areas on the riverbed generating their own acoustic signal. Each area is considered an independent acoustic source depicting continuously all the noises generated by bedload impacts within the defined area. Hence, the total SGN signal depends on the particle-particle

85 impact signal as well as the number of impacts in each area. Assuming that the impacts are random in space and time, the signal powers are considered to have an additive effect (Vér and Beranek, 2007).

The transported bedload is a mixture of sediments impacting the riverbed with different impact rates and intensities depending on the particle diameter, fractional bedload flux, and hydraulic conditions. In this case, the source power spectral density (PSD, the variation of power with frequency) per unit area s (in $Pa^2 \cdot Hz^{-1} \cdot m^{-2}$) is computed using a linear system that weights

90 the source energy spectrum e ($Pa^2 \cdot s \cdot Hz^{-1}$) generated (at a distance $r = 1$) due to impacts of particles of diameter D_k with the corresponding impact rate η (number of impacts per second per unit area):

$$s\,(f, r = 1) = \sum_{k=1}^{N_D} \eta(D_k, q_s) \cdot e(f, D_k, r = 1) \quad (1a)$$

$$\eta(D_k, q_s) \propto q_s \,.\, \beta\,(D_k) \quad (1b)$$

Where, N_D is the number of classes in the bedload mixture, q_s is the specific bedload flux (g/s/m), β is a coefficient dependent on particle saltation trajectory, which is calculated using different empirical equations as a function of particle size, bedload grain-size distribution, and hydraulic conditions (such as water depth and riverbed slope) (Auel et al., 2017; Gimbert et al., 2019; Lamb et al., 2008b, etc.). Equation (1) shows a linear relation between SGN source s and the specific bedload flux q_s through the impact rate term η. Then the source profile can be considered a proxy of the spatial variability of bedload flux in the river cross-section.

2.2 Transmission loss function

Several processes in rivers are responsible for acoustic waves' attenuation and power losses. The acoustic waves can be attenuated by geometric spreading, refractions or diffractions depending on the geometry of the propagation medium (Geay et al., 2017; Rigby et al., 2016), roughness (Wren et al., 2015), and impedance (Etter, 2018) of the riverbed. Moreover, the presence of water turbulence and entrained air bubbles induce significant attenuation of acoustic waves (Field et al., 2007). In shallow water columns such as in rivers, low-frequency acoustic waves are trapped and undergo reflection between the riverbed and the water surface as in a Pekeris waveguide (Pekeris, 1948). In this case, acoustic waves with low frequency are scarcely propagated with a limit frequency called cut-off frequency (f_{cutoff}), below which waves don't propagate (Geay et al., 2017; Rigby et al., 2016). This cut-off frequency is inversely proportional to the riverbed material's, water level and sound celerity. For example, for a river section with 0.5 m and 2000 m/s as average celerity of sound in sediments (Hamilton, 1987), the cut-off frequency is approximately 1.1 kHz which is lower than bedload SGN frequency with a range of particle diameters less than 100 mm (Thorne, 2014).

For frequencies above the cut of frequency, a transmission loss function (TL) is defined to assess the attenuation of bedload SGN wave signal in river. The TL function depicts the power losses of an acoustic signal propagated from an acoustic source position to any position in the river. Experimental work by Geay et al. (2019) proposed that the propagation function is a combination of a geometrical spreading function TL_1, and a frequency-dependent function TL_2 that describes the losses of acoustic waves due to the scattering and absorption effects of the river:

$$TL(f,r) = TL_1(r).TL_2(f,r), \quad (2)$$

The function TL_1 depicts the decrease of the acoustic power as the waves spread and diverge with propagation away from the source. For this function, a simplified rectangular geometry of a river section with constant water depth is considered. Depending on the riverbed and water surface interface behavior, two propagation models can be defined. First, if the interfaces act as perfect absorbers (no reflections), the acoustic waves propagate in a spherical mode as in free space (Eq. 3a). Second, if the interfaces are perfect reflectors, the acoustic waves are trapped between the two interfaces and propagate in a cylindrical way (Eq. 3b).

$$TL_{1,s}(r) = \frac{1}{r^2}, \quad (3a) \qquad TL_{1,c}(r) = \frac{2}{rh}, \quad (r > h) \quad (3b)$$

125 Where $TL_{1,s}$ and $TL_{1,c}$ are the geometrical spreading function for spherical and cylindrical models, respectively, and r is the source-hydrophone distance (in m). The attenuation and losses induced by all other effects and processes, such as water turbulence, are estimated by an exponential propagation function (TL_2):

$$TL_2(f) = e^{-2\alpha(f)r}, \quad (4)$$

Where $\alpha(f)$ is a frequency-dependent attenuation coefficient (m^{-1}), assumed to vary linearly with the frequency above the

130 cut-off frequency (Jensen et al., 2011) and can be written as follows:

$$\alpha(f) = \alpha_\lambda \cdot \frac{f}{c_f}, \quad (5)$$

Where α_λ is a dimensionless attenuation constant characterizing the propagation in the river, with high values corresponding to poor propagation conditions (or higher attenuation of the signal), and c_f celerity of sound in water. Geay et al. (2019) proposed a protocol for in-situ characterization of α_λ, which consists in emitting a known calibrated acoustic source (with a

135 loudspeaker) from a fixed point of the river cross-section and measuring the losses of acoustic power per frequency band, with distance. The attenuation coefficient can then be fitted using the measurements for both the spherical (α_{λ_s}) and cylindrical (α_{λ_c}) models. They applied this protocol to seven rivers and concluded that α_λ, is positively correlated in the first place with the riverbed slope and roughness. Thus more attenuation is expected in steep and rough rivers where more flow turbulence is induced.

140 Propagation has mainly been studied in the marine environment (Roh et al., 2008). For a source in a waveguide, spherical spreading is dominant in the near field. It then transits toward cylindrical spreading when moving away from the source, and cylindrical spreading is dominant in the far field (Jensen et al., 2011). These physical properties have been poorly investigated in rivers, but Geay et al. (2019) show consistent results with TL calibrated with the spherical and cylindrical model converging at the far field. Because we measure the bedload SGN as close as possible to the noise sources (see section 4.2), we assume in

145 the following that our acoustic measurements are more dominated by spherical propagation from the near field. This hypothesis is supported by Nasr et al. (2021), which shows a better global performance of the spherical propagation model when compared to the cylindrical one.

2.3 Bedload SGN source

Let's consider an acoustic signal generated from a given point source in the space, with a power spectral density s (PSD, in

150 $\mu Pa^2 \cdot Hz^{-1}$) that propagates to different positions in the river. The signal with PSD $\wp(r)$ (in $\mu Pa^2 \cdot Hz^{-1}$) measured at a distance r from the point source is calculated as the product between the acoustic source spectral power s and the transmission loss function TL (Eq. 6a). However, in the case of surfacic acoustic sources s (in $\mu Pa^2 \cdot Hz^{-1} \cdot m^{-2}$), as defined for SGN, propagation is calculated as a function of area double integral with variable r (Eq. 6b).

$$\wp(\text{f}, \text{r}) = \text{s}(f) \cdot TL(f, r), \quad (6a)$$

155

$$\wp(f, x_{hyd}, y_{hyd}, z_{hyd}) = \iint_{x_{s1}, y_{s1}}^{x_{s2}, y_{s2}} s(f, x, y) \cdot TL(f, r(x, y)) dx dy \quad (6b)$$

Where $s(x, y)$ is the source power function which defines the spatial variability of the source in the river, and $r(x, y) =$

$\sqrt{(x - x_{hyd})^2 + (y - y_{hyd})^2 + (z - z_{hyd})^2}$ is the distance function between any point on the riverbed and the hydrophone

positioned at coordinate $(x_{hyd}, y_{hyd}, z_{hyd})$. The integral limits $(x_{s1}, y_{s1}, x_{s2}$ and $y_{s2})$ define the boundaries of the source in

space.

160 Figure1 illustrates the attenuation of an acoustic signal by the spherical transmission loss function for a uniform square unit

area acoustic source s ($\mu Pa^2 \cdot Hz^{-1} \cdot m^{-2}$). This realistic source s was constructed with the Nasr et al. (2021) model for a

bedload mixture composed of grains uniformly distributed in the range [1-100 mm], with a specific flux of 1000 g/s/m, and

for a river with 1% slope and 1m water level. A value of $\alpha_{\lambda_s} = 0.1$ is used, and two additional values $\alpha_{\lambda_s} = 0.01$ and 0.001

are also considered for r= 2m. Figure 1b presents the power spectral density PSD (obtained by Fourier transform) of the source

165 s (in blue) and the propagated signal $\wp$ (in red). The losses with increasing distance due to the geometrical transmission loss

function $TL_{1,s}$ is evident when comparing the different curves at 2, 5, and 10 m. Simulations at r=2m with different α_{λ_s}

values also illustrate different losses at higher frequencies, captured by the TL_2 function (Eq. 5).

Moreover, we observe a total shift of spectrum to the lower frequencies with distance due to the TL_2 function and the increasing

attenuation coefficient with frequency (eq. 5). The vertical green lines correspond to the central frequencies f_c (defined by the

170 condition $\int_0^{f_c} |\wp(f)|^2 df = \int_{f_c}^{\infty} |\wp(f)|^2 df$) calculated for each power spectrum $\wp$. Between the source position and 10 m,

the central frequency decrease from 4.5 kHz to 1.5 kHz. This result illustrates, in particular, how the estimation of transported

grain size, which depends mainly on the spectral content, can be misleading without considering the propagation effect.
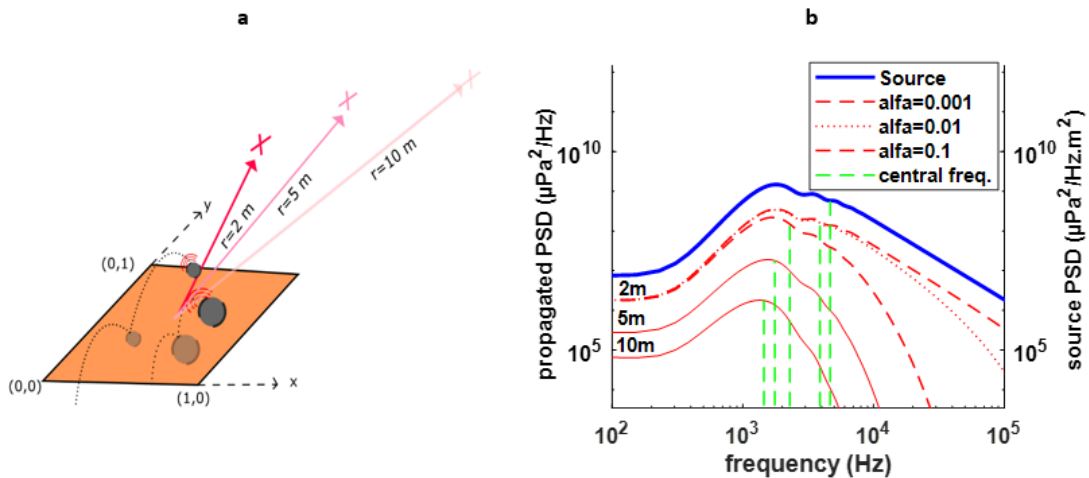
Figure 1 a) representation of a surfacic acoustic source with multiple particle-particle impacts. b) The power spectral density of the
175 **modelled source signal (r=1 m), with the propagated signals to r=2,5, and 10 m. The green vertical lines represent the central**
frequency of each PSD.

3 SGN source inversion method

This section presents the general formulation of the inverse mathematical problem.

3.1 Problem formulation

180 The purpose of the inversion problem is to estimate the PSD and the spatial distribution of bedload SGN sources in rivers. The problem can be illustrated in Figure 2, where M bedload SGN sources are assumed to be distributed on the riverbed with the same width $W_M = W/M$. It is assumed that the specific bedload flux ($\bar{q}_{s,x}$) is constant for each band in the streamwise direction (along longitudinal line y); in other words, a source is assumed uniform along a given longitudinal line. This simplifies the geometry of sources as planar strips with infinite lengths in the y direction (Figure 2). The PSD per unit area

185 $s_m(f)$ ($\mu Pa^2 \cdot Hz^{-1} \cdot m^{-2}$) is defined for each source with m an integer $1 \leq m \leq M$. The vector $\boldsymbol{S}$ of dimension [M,1] and with the elements $s_m(f)$ represent all the sources' PSD distributed in the river.

For solving the problem, the first parameter to be considered is the acoustic measurements of the bedload SGN. Here, we consider a situation matching the drift boat measurement, where a boat supporting the hydrophone successively measures the associated acoustic SGN at N different positions (Geay et al., 2020). N acoustic measurements are thus assumed to be

190 distributed on the river cross-section (x direction), from which we compute N PSD. The parameter $p_n(f)$ corresponds to the PSD measured at the nth position with n an integer $1 \leq n \leq N$. The measured SGN profile is thus represented by the vector $\boldsymbol{P}$ with dimension [N,1] comprising all measured $p_n(f)$.

Given all sources in the river, the measured $p_n(f)$ is the contribution of the M acoustic sources to the nth measuring position, such that:

195
$$p_n(f) = \sum_{m=1}^{M} a_{m,n}(f) \cdot s_m(f) \quad (7)$$

Where $a_{m,n}$ is the attenuation factor (calculated for a surfacic source using the frequency-dependent transmission loss function TL), that affects the signal of source m when measured by the hydrophone at position n:

$$a_{m,n} = \iint_{x_{m1},y_{m1}}^{x_{m2},y_{m2}} TL\big(f(k), r_{m,n}(x,y)\big) dx dy \quad (8)$$

Where $r_{m,n}$, is the function that defines the distance between any point within the source m area and a hydrophone at position

200 n with coordinate ($x_{hyd,n}, y_{hyd,n}, z_{hyd,m}$) such that $r_{m,n}(x,y) = \sqrt{\left(x - x_{hyd,n}\right)^2 + \left(y - y_{hyd,n}\right)^2 + \left(z - z_{hyd,m}\right)^2}$, and z depends on the geometry of the section. The integral limits x_{m1}, y_{m1}, x_{m2} and y_{s2} define the boundaries of the source in space. The values of y_{m1} and y_{m2} were chosen to be much greater than the river width W (length = 10W) to model the infinite length of the source stripe. Finally, when Equation 7 is applied to the whole domain we obtain the matrix:

$$\boldsymbol{P} = \mathcal{A} \cdot \boldsymbol{S} \quad (9a)$$

205

$$\begin{pmatrix} p_1(f) \\ \vdots \\ p_N(f) \end{pmatrix} = \begin{pmatrix} a_{1,1}(f) & \cdots & a_{M,1}(f) \\ \vdots & \ddots & \vdots \\ a_{1,N}(f) & \cdots & a_{M,N}(f) \end{pmatrix} \cdot \begin{pmatrix} s_1(f) \\ \vdots \\ s_M(f) \end{pmatrix} \quad (9b)$$
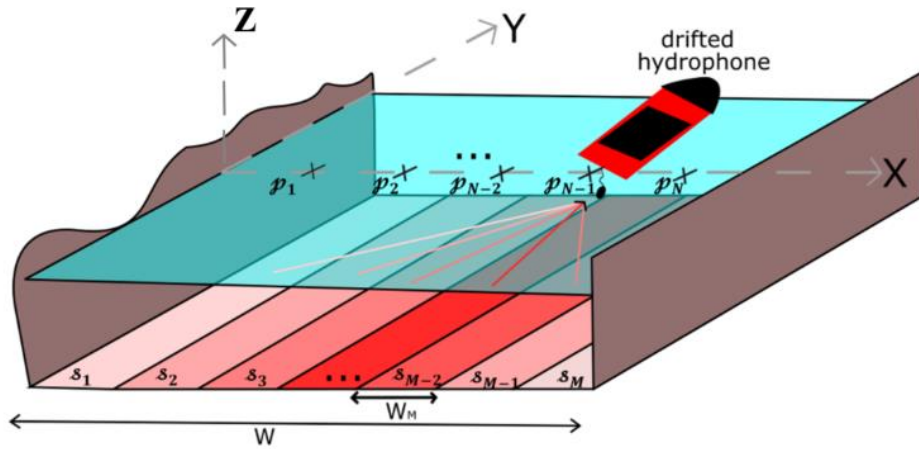
Where $\mathcal{A}$ is the attenuation matrix.

Figure 2 Comprehensive presentation of the inversion problem geometry.

210 **3.2 Solution to the inversion problem**

At this stage, we consider that we know the measured acoustic matrix $\mathcal{P}$ and assume that the attenuation matrix $\mathcal{A}$ is computed (Eq.3 and 4) with a known (measured) attenuation term α_λ. We seek the solution $\widehat{\mathbf{S}}$ of the vector $\mathbf{S}$, which allows the best fit of the measured $\mathcal{P}$ to the modeled acoustic matrix $\widehat{\mathcal{P}} = \mathcal{A} \cdot \widehat{\mathbf{S}}$. A traditional approach for this type of problem is the Least Square (LS) method, with an optimization algorithm that works on the minimization of squared residual errors between $\mathcal{P}$ and

215 $\widehat{\mathcal{P}}$. The error vector $\boldsymbol{\epsilon}$ can be written as in Eq. 10a, and the optimization of the problem solving $\widehat{\mathbf{S}}$ is presented in Eq. 10b, where the argument of the minimum of $\boldsymbol{\epsilon}$ ($\arg\min(\boldsymbol{\epsilon})$) is the value of $\widehat{\mathbf{S}}$ that minimize $\boldsymbol{\epsilon}$.

$$\boldsymbol{\epsilon} = \mathcal{P} - \widehat{\mathcal{P}} = \mathcal{P} - \mathcal{A} \cdot \widehat{\mathbf{S}} \quad (10a), \qquad \widehat{\mathbf{S}} = \arg\min(\boldsymbol{\epsilon}) \quad (10b)$$

The relation between the number of sources M and measurements N determines the algebraic solution type of the problem in Eq. 9. If the number of sources exceeds the number of measurements ($M > N$), then the equation is considered under-

220 determined. In this case, there are more unknowns than the number of the equation and an infinite number of solutions of $\widehat{\mathbf{S}}$ exists. On the other hand, if $M < N$, there are more independent equations than unknowns, and the equation system is considered over-determined. In the latest case, it is shown by Nelson and Yoon (2000) that the optimal solution for the acoustic source vector, which ensures minimization of Eq. 10b is :

$$\widehat{\mathbf{S}} = \mathcal{A}^+ \cdot \mathcal{P} \quad (11)$$

225 Where $\mathcal{A}^+ = (\mathcal{A}^t \cdot \mathcal{A})^{-1} \cdot \mathcal{A}^t$ is the pseudo-inverse of the matrix $\mathcal{A}$ and $\mathcal{A}^t$ is the transpose matrix.

The pseudo-inverse algorithm for non-square matrixes exhibits a common drawback where the solution $\widehat{S}$ may suffer from instability under slight variations of $\mathcal{A}$ or $\mathcal{P}$. The problem's ability to estimate stable or non-stable solution $\widehat{S}$ is called conditioning of the problem. The conditioning of the problem is quantified by the condition number σ of the matrix $\mathcal{A}$ to be inversed. This condition number is defined as $\sigma(f) = \|\mathcal{A}\| \cdot \|\mathcal{A}^-\|$ where $\|\mathcal{A}\|$ is the 2-norm of the matrix $\mathcal{A}$ (Golub and Van

230 Loan, 1996). A system with a high value of σ is considered an ill-conditioned system that generates high instability of the solution $\widehat{S}$ to small deviation or error in $\mathcal{A}$ and $\mathcal{P}$. In contrast, a value σ closer to 1 is a well-conditioned system. A problem with a condition number $\sigma < 10^3$ can be considered a well-conditioned (Arthur et al., 2017).

In addition, relatively high resolution of hydrophone measurements (N>>M, or close measurements) will lead to matrix $\mathcal{A}$ with close row values and, consequently, rank deficient matrix. A classical solution for such instability problems is the non-

235 negative least square (NNLS), a constrained least squares problem where the coefficients are not allowed to become negative. In the case of a number of sources equal to the number of measuring points (N=M), then the pseudo-inverse matrix is simply the algebraic inverse matrix of $\mathcal{A}$ and $\widehat{S} = \mathcal{A}^- \cdot \mathcal{P}$.

The Matlab function *lsqnonneg()*, which follows the NNLS algorithm, is used for solving the inversion problem.

3.3 Numerical testing of the inversion model

240 Several numerical tests are presented here to illustrate the behavior and limits of the proposed inversion model. The tested section is composed of a 10 m wide river, with a rectangular section and a 1-meter water depth. Bedload SGN sources are assumed to be distributed on the riverbed in the form of bands, as in Figure 2. The considered length of the sources along the river direction is 100m upstream and 100m downstream of the section. Several distributions of bedload active channels—the section with bedload transport—are tested (single, dual, and triple channels). The total bedload active channel width in the

245 three configurations equals 4 m. Within the active bedload channel, the source PSD s_m is computed with Nasr et al. (2021) (blue curve in figure 1b); outside s_m is zero.

We consider the number of simulated acoustic measurements equal to the number of sources (M=N), and the measurements are positioned above each source's center. The simulated PSD p_n are calculated using equation 7. The spherical propagation model is used with an attenuation coefficient $\alpha_{\lambda_s} = 0.05$ (equivalent to propagation environment for a river with slope $S \approx$

250 1%).

Figure 3 shows the cross-sectional distribution of the frequency-integrated source power P_{s_m} ($\mu Pa^2 \cdot m^{-2}$, in blue line) and simulated measured power P_{p_n} (μPa^2, in red line) for different configurations, such that:

$$P_{s_m} = \int_{f_{min}}^{f_{max}} s_m(f)\, df, \quad (12a) \qquad P_{p_n} = \int_{f_{min}}^{f_{max}} p_n(f)\, df, \quad (12b)$$

In the absence of hydraulic noises at low frequencies (Geay, 2013), $f_{min} = 0\ kHz$ and $f_{max} = 150\ kHz$, which is the

255 maximum value of the simulated PSD.

In the first place, no out extrinsic acoustic noise has been considered. Using the simulated acoustic profile $\mathcal{P}$ and equation 11, the sources PSD are inversed by NNLS method for different tests. Figure 3 shows that the inversed power profiles $\widehat{P_{s_m}}$ (in black line) coincide with generated profile (in blue) for all tests suggesting good prediction and solution of NNLS under accurate measuring conditions.

260   To account for possible uncertainty in field measurements, a noise has been added to the simulated $\wp_n$. The noise was added in the form of random coefficients in space and frequency bands, multiplied by the simulated PSD of $\wp_n$. The resulting acoustic profiles are plotted (dashed red lines) in Figure 3. In the presence of noise, the inversed source power $\widehat{P_{s_m}}$ (dashed black lines) is no longer similar to the imposed one. The results errors are not only limited to the intensity of sources but also the appearance of sources outside the bedload active channel. Nonetheless, the average cross-sectional power of the inversed source profile

265   (integration of the curve divided by the width) is between 2.35-2.43 μPa^2/m, which is close to the corresponding value for that for the imposed source (2.36 μPa^2/m). This means that if we consider the total inversed power, the error is more limited to the localization of these sources.

To numerically assess the results, a variance-explained accuracy measure ($VEcv$) parameter is introduced (Li, 2017). The advantage of the accuracy measure $VEcv$ is that it is unit/scale, data mean, and variance independent according to its definition.

270   A $VEcv$ close to one means good accuracy of the model. The $VEcv$ us calculated as follow:

$$VEcv = \left(1 - \frac{\sum_{m=1}^{M}\left(P_{s_m} - \widehat{P_{s_m}}\right)^2}{\sum_{m=1}^{M}\left(P_{s_m} - \overline{P_s}\right)^2} \right), \quad (13)$$

Where, $\widehat{P_{s_m}}$ is the inversed source power, P_{s_m} is the imposed source power, $\overline{P_s}$ is the average of all imposed source power. The values of $VEcv$ have been calculated for each simulation and are presented in the titles of Figure 3. The $VEcv$ values show that the inversion model has a good performance even in the presence of noise ($VEcv \approx 0.9 - 0.6$). However, the $VEcv$ values

275   noticeably decrease when the number of bedload active channels increases, suggesting a higher sensitivity of the model to field uncertainty under complex bedload distribution.
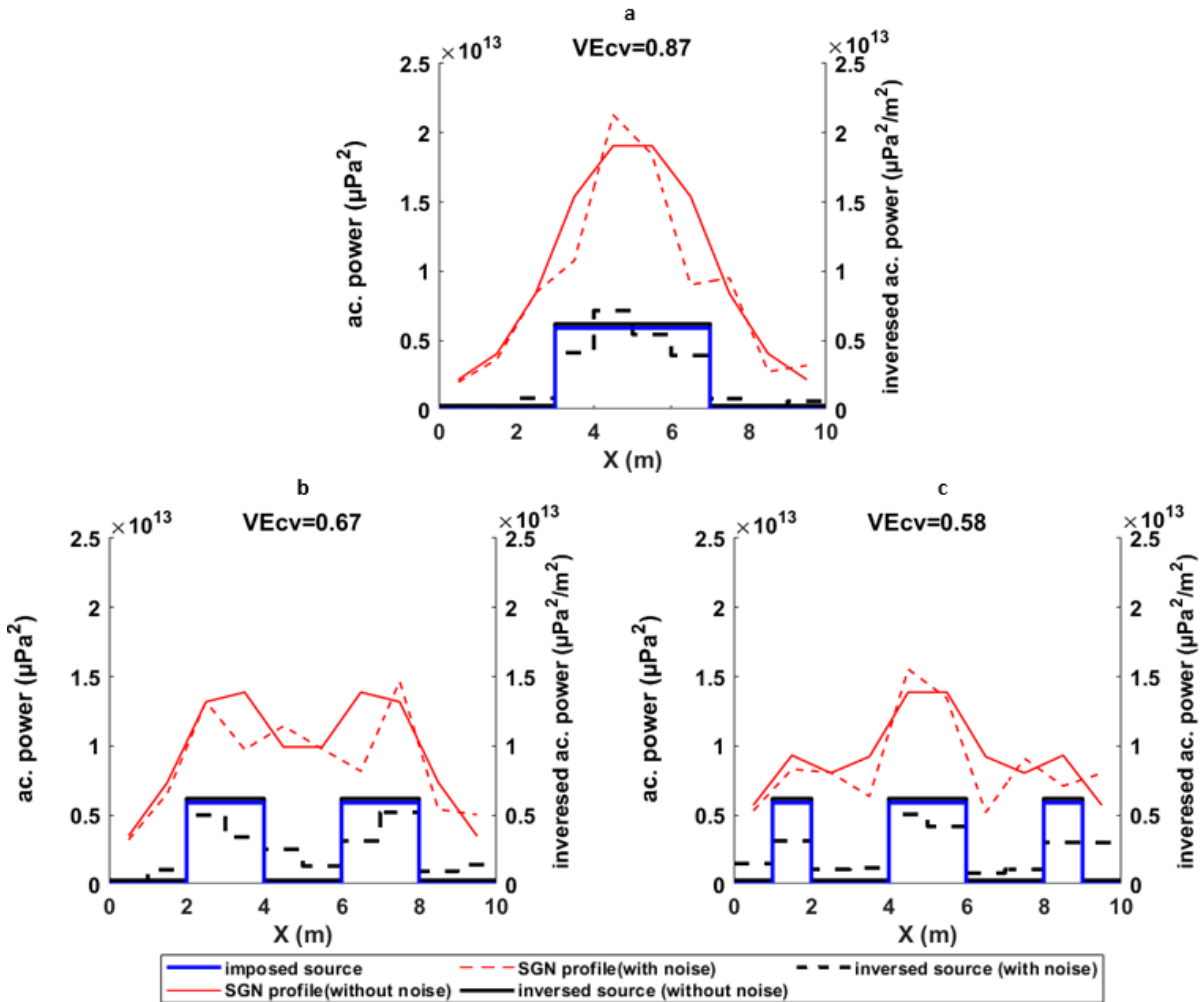
Figure 3 Numerical test results of the inversion model for a) single, b) double, c) triple channel configuration. The figures present the variation of acoustic power for the source ($\mu Pa^2 \cdot m^{-2}$) and for simulated SGN profile (μPa^2) in
280 **the river cross-section.**

4 Inversion model validation

4.1 Validation with active test measurements

This first experiment aims to test the inversion model under controlled source conditions. It is technically challenging to deploy a sound source with a scale comparable to SGN source in the river. Instead, in this experiment, we use a loudspeaker in the
285 river as a source with a known signal and location. The test consists of measuring the emitted sound by the loudspeaker at different locations in the river and then testing the ability of the inversion model to retrieve the active source's location and PSD.

4.1.1 Isere river and experimental setup

290   This experiment was carried out in the Isere river in south-eastern France. The measuring site is located next to Grenoble city (45°11'55. .0"N 5°46'11.4"E) on a pedestrian's footbridge crossing the river. The local average slope for the measured section is 0.05% with 60 m width, and the annual average flow is 180 $m^3 \cdot s^{-1}$. The riverbed is composed of gravel with average $D_{50,bed} = 23\ mm$ measured with the Wolman (1954) sampling protocol for the exposed riverbed. During the time of measurement, in the 25th of August 2022, the average flow was 110 $m^3 \cdot s^{-1}$. Under this flow condition the Isere river was

295   characterized by low hydraulic noises generated by the flow turbulence at low frequencies (Geay, 2013).

We used a waterproof piezoelectric loudspeaker Lubell with a 23 cm diameter (model LL916H; http://www.lubell.com/LL916.html), characterized by a quasi-flat (+/-10dB) frequency response between 500Hz-21,000Hz. The loudspeaker is connected to an emission RTSys system (TR-SDA14) which controls the emitted signal by a ".wav" file stored inside the RTSys. The chosen transmission signal is a logarithmic frequency modulation between 500 Hz and 21 000

300   Hz in 0.25 seconds. The ".wav" file for the sound emitted by the loudspeaker is provided in the supplementary material. The loudspeaker signal was characterized in a lake next to Grenoble city in France. The source was positioned at a distance of around 3 m from the water's surface. The emitted signal was measured at a 1m horizontal distance from the source with an HTI-99 hydrophone (High Tech, Inc.,http://www.hightechincusa.com), characterized by a flat frequency response ($\mp$ 3dB) between 2 Hz and 125 kHz. Different orientations of the loudspeaker in space have been tested. A PSD ($\mu Pa^2 \cdot Hz^{-1}$) was

305   calculated for each measured chirp. Finally, using equation 6b, the surfacic PSD of the loudspeaker ($\mu Pa^2 \cdot Hz^{-1} \cdot m^{-2}$) was calculated by dividing the measured PSD with the TL function term. The TL function was calculated considering the dimension of the source for r=1m, and $\alpha_{\lambda_s} = 0$, attenuation being only due to geometrical spreading in a lake. The result of the source surfacic source power is presented in Figure 4c (green lines) with the 5%, 50% 95 % percentiles.

In the Isere river, the loudspeaker has been deployed from the bridge to the riverbed at the position x_{source}=48 m and y_{source}=3

310   m (in the downstream direction). At this position, the average water column depth is 1.5 m. The signals were emitted from the source in an endless loop. We measured the acoustic profiles every 2 m between x =8 and x =56, with the same hydrophone and acquisition system presented above. The protocol was identical to Geay et al. (2020), with the hydrophone mounted on a floating river board (40cm below the water surface), and freely drifted from the bridge (drift position between y =2m and y =4m from the bridge). For each drift n located at x_n, we measured the power spectrum of all signal impulsion during the drift

315   and determined the median spectrum PSD_n. Each drift n is now characterized by its coordinate$(x_n, y_n = 3m)$, and a median spectrum PSD_n.

Inversion of the active acoustic source requires the definition of parameters presented in equation 9 ($\boldsymbol{\mathcal{P}}, \boldsymbol{S}$ vectors and $\boldsymbol{\mathcal{A}}$ matrix). For the measured acoustic profile, the vector $\boldsymbol{\mathcal{P}}$ is composed of the 25 measured median power spectrum defined above, $\wp_n(f) = PSD_n(f)$ (1< n <25). We consider $N = M$ =25 and incorporate 25 square sources of 2-meter side distributed

320 between $7 \leq x \leq 56$, with an unknown source power spectrums $s_m(f)$. The transmission loss parameters $a_{m,n}(f)$ are calculated using equation 8 for the spherical model. The attenuation coefficients, $\alpha_{\lambda_s} = 10^{-4}$ have been estimated following the protocol proposed by Geay et al. (2019) during the measurements day. The source spectrum $s_m(f)$ are calculated using the third-octave band of the measured spectrum.

The area of the sources in this application is 4 m^2 ($2m$ side squares) which is different than that of the loudspeaker area ≈ 0.4

325 m^2. In this case, an area ratio correction coefficient is applied to the inversed results in order to compare it with the loudspeaker source signal measured in the lake. The ratio is between the TL function calculated as in Eq. 6b for the inversed source area and for the loudspeaker area.

4.1.2 Results

Figure 5b plots the measured acoustic power profile P_{p_n} (in red line), calculated with Eq.12 between frequencies of 500-

330 21000 Hz. The measured spectrums show different intensities depending on the distance from the active source. No significant variation in the spectral distribution is observed with propagation due to the relatively low attenuation coefficient in the Isere river.

The results of the inversed power profile $(\widehat{P_{s_m}})$ are plotted in Figure 5b (black line). The results show that the inversion model successfully captures the active source location between x=47 and x=49 ($m = 21$). However, some residual sources have been

335 modeled mainly around the active source location and at other locations in the river. As in the numerical test with noise (section 3.3), it is suspectable that measurement uncertainty contributes to such residual sources as they coincide with the perturbation in the measured acoustic profile (ex x= 26 and 35 m).

The spectrum of each drift ($p_n(f)$) are presented in Figure 5c (continuous faded lines), and the color index corresponds to the distance of the spectrum from the deployed loudspeaker. Figure 5c shows as well the inversed source spectrum in the proximity

340 of the loudspeaker location $\hat{s}_{n=21}$ (between x=47 and x=49). The results show that the inversed spectrums are comparable with the lab-measured spectrum, which fits within the 5%-95% percentiles on most frequencies.

The residual errors of the inversion model have been estimated by reconstructing the measured signal using the estimated $\widehat{s_m}(f)$ and equation 7. The reconstructed power profile $\widehat{P_{p_n}}$ is presented in Figure 5b (dashed black lines), which shows a good visual agreement with the measured power profile P_{p_n} (in red). The VEcv calculated for the profile $\widehat{P_{p_n}}$ referenced to P_{p_n} is

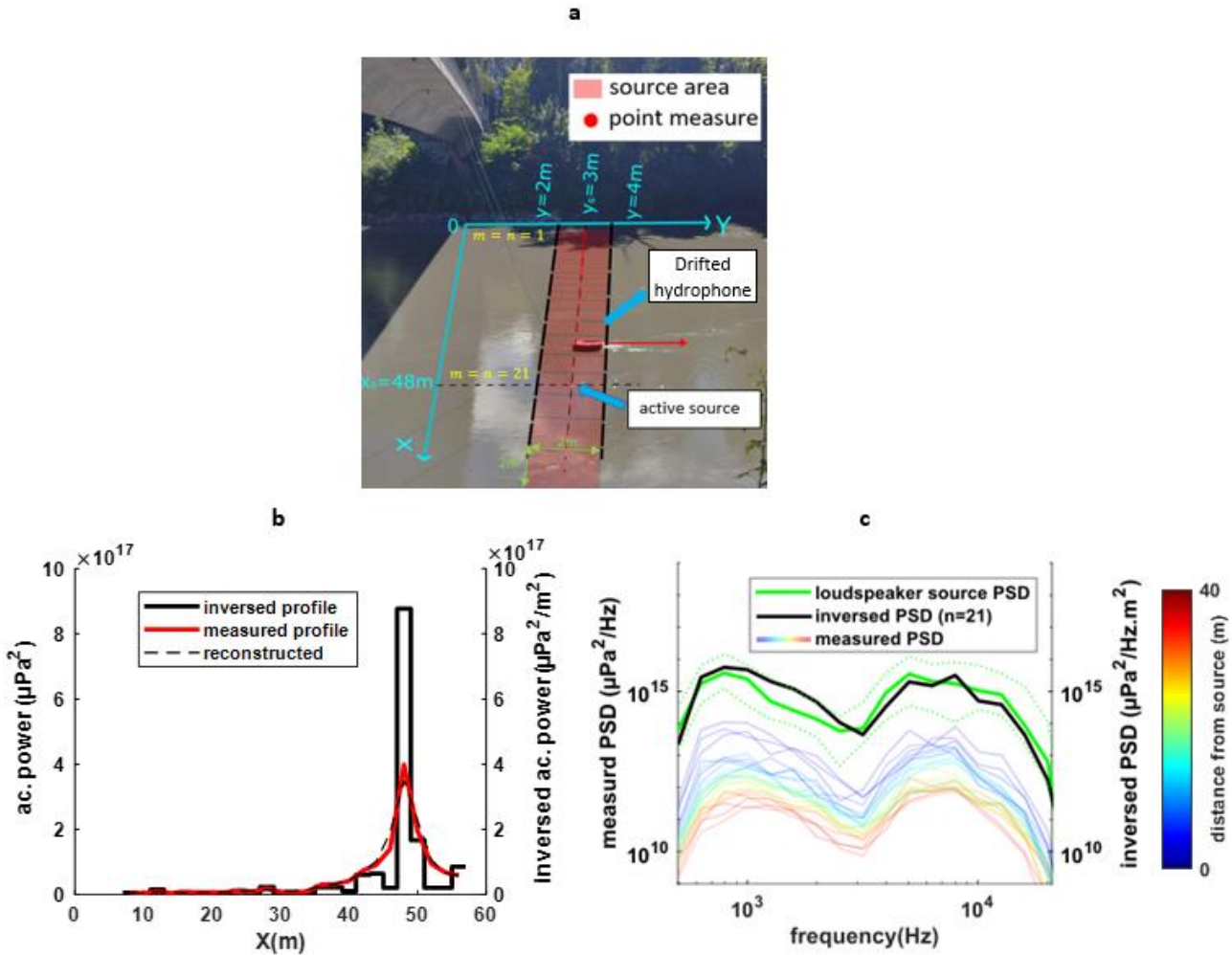345 VEcv=0.94 which shows a good performance of the spherical model to reconstruct the measured profile.

Figure 4 a) Representation of the geometry of sources and acoustic measurements on the Isere river. **b)** measured acoustic power (μPa^2, continuous black line) and the inversed source power ($\mu Pa^2 \cdot m^{-2}$, , continuous red line). The dashed red line corresponds to the reconstructed acoustic power profile using the inversed source profile and Eq. 9. **c)** measured spectrum at each position in the river ($\mu Pa^2 \cdot Hz^{-}$, continuous fadedlines). The color index indicats the distance of the measurement from the source which increases from blue to red. The mean inversed spectrum ($\mu Pa^2 \cdot Hz^{-} \cdot m^{-2}$, in red line) corresponds to the spectrum at location 47-49 m (n=21). The green spectrum corresponds to the median of the lake measured spectrum with the dotted line corresponds to 5% and 95% percintiles.

4.2 Validation with passive SGN measurements

4.2.1 Giffre river and experimental setup

350   In this part, we apply the inversion model to bedload SGN measurements. The experiment was carried out in the Giffre river

located in French Alps. The measured section is on a pedestrian crossing bridge (46°04'48.8"N 6°42'19.4"E). The average

slope of the section is 0.3% and 29 m in width. Two SGN and bedload flux measurements were carried out during the melting season on 13th of June 2018 and 6th of July 2021. On these dates, the flow discharges were 50 m^3/s and 26 m^3/s respectively with 0.9 m and 0.7 m average water depth.

355   Acoustic measurements were obtained using HTI-99 hydrophones (with sensitivity: -200.1 dB in 2018 and -199.8 dB in 2021) and RTSys acquisition system with the drift protocol (Geay et al., 2020). The drifts were 20 to 30 meters long (in the y direction) with the hydrophone setup 30 cm below the surface. Several repetitions of drifts have been performed at each cross-sectional position x_n to account for measurement uncertainty and temporal variability. Similarly to the active test, the pressure signal has been treated in the frequency domain. For each drift at the location x_n, we computed the median $PSD_n(f)$. In the

360   presence of repetition of drifts at the same location x_n, we averaged the PSD_n.

Bedload particles were sampled from the bridge using a handheld Elwha sampler of dimensions 203 × 152 mm (figure 6a). Sampling was performed at various cross-section positions following the procedures proposed by Edwards and Glysson (1999) with variable repetitions. Each sample was dried, sieved, and weighed to calculate the transport rate and grain size distribution (GSD). We obtain a specific bedload flux $q_{s,i}$ (in $g \cdot s^{-1} \cdot m^{-1}$) calculated as follows:

365

$$q_{s,i} = \frac{m_i}{t_i \times W_{\text{sampler}}}, \quad (15)$$

Where W_{sampler} is the inlet width of the sampler, m_i and t_i are the mass and the duration of sampling respectively. The average bedload flux profile has been calculated within N widows, each of 2 meters in width. Each window is centered on an acoustic point measurement x_n as for the acoustic source. The average bedload flux $\bar{q}_{s,n}$ (in $g \cdot s^{-1} \cdot m^{-1}$) for the widow n is calculated by averaging the values of $q_{s,i}$ contained inside the spatial window n.

370   For solving the inversion problem, we use a geometry similar to figure 2. The length of the sources is extended between $y =$ -150 m and $y =$ 150 m accounting for the assumed infinite length of the SGN source.

Two active tests have been carried out to characterize the propagation environment in the Giffre River during the two measurement days in 2018 and 2021. The attenuation coefficients estimated for the spherical model are $\alpha_{\lambda_s} = 0.006$ and $\alpha_{\lambda_s} = 0.004$ for 2018 and 2021 respectively. The attenuation coefficient is measured up to a maximum frequency of 20 kHz

375   and extrapolated at higher frequencies assuming a linear regression.

4.2.2 Results

Figure 5 presents the punctual measurements and the averaged profile for bedload flux and acoustic measurements for both experiments. The left and right riverbanks are located at x=0 and x=29, respectively. In both measurements, the bedload flux profile is composed of a main transported channel localized at the right section of the rive (peak at x=20). The average specific

380   bedload flux calculated for both experiments shows that the bedload transport intensity in 2018 was fifteen times more than that of 2021 (328 g/s/m compared to 22 g/s/m). The measured SGN profiles show a coherent variation of acoustic power with

the bedload flux in the river cross-section. However, the decrease of the acoustic power in the left part of the river section does not correspond to the same intensity decrease of bedload flux.

Acoustic recording samples from both experiments are presented in the supplementary materials. After a qualitative analysis
385 of the recordings, bedload SGN can be clearly heard above 800 Hz. At frequencies lower than 400 Hz, the main source of noise is the hydraulic noise induced by the flow turbulence in the river and around the hydrophone. The mean measured PSD are presented in Figure 6a and 6b. The central frequencies, calculated for the mean PSD are 5.6 kHz and 10 kHz for 2018 and 2021 respectively. The difference of central frequency is mainly induced by the different grain-size distributions sampled during both experiments (the average D_{50} sampled in 2018 was 6.8 mm and 3 mm in 2021). In addition, the attenuation of the
390 SGN signal is more important during 2018 measurements due to higher flow which can induce more water turbulence.
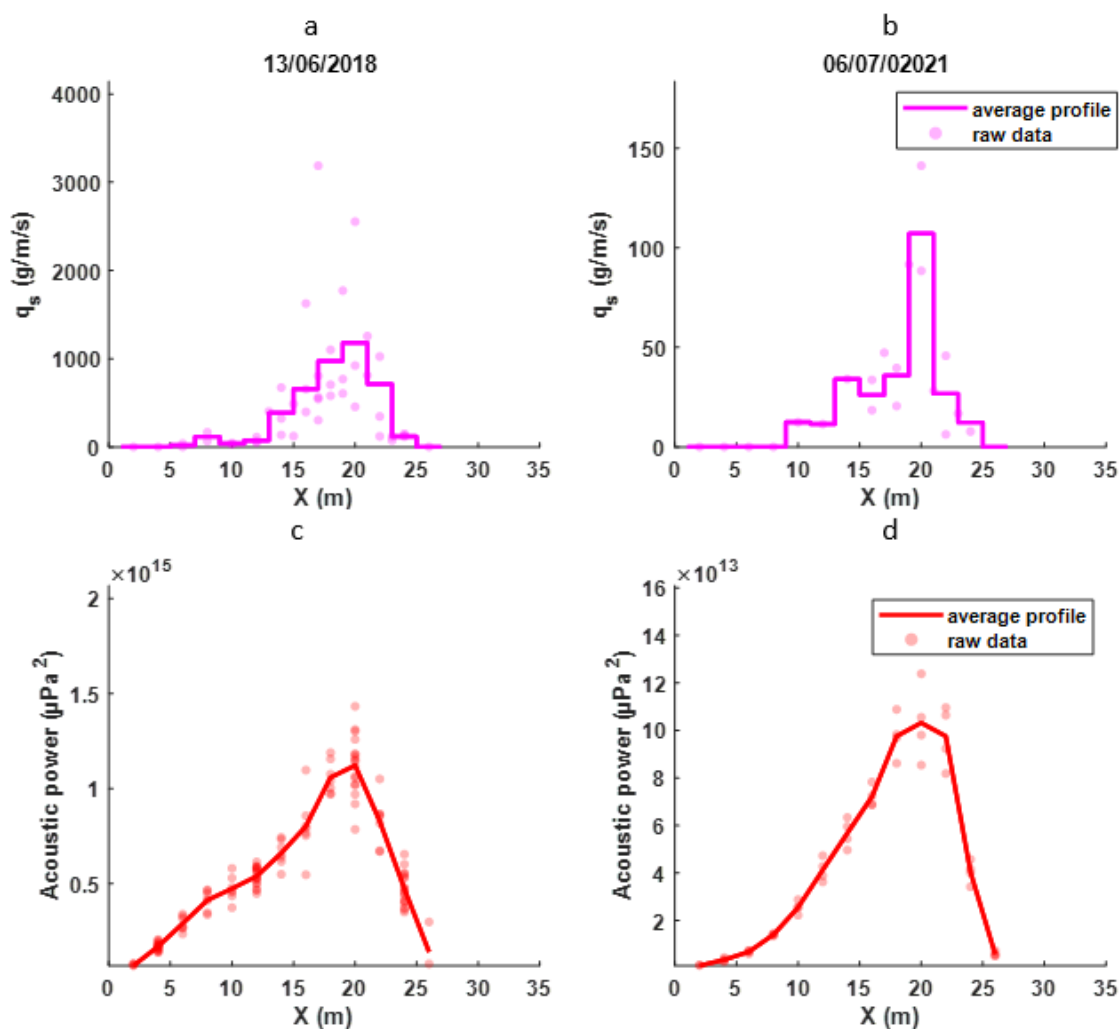

Figure 5   Measured bedload flux a) in 2018 experiment and b) in 2021 experiment. The measured acoustic power a) in 2018 experiment b) in 2021 experiment.

Figures 6a and 6b also present the mean inversed PSD. The central frequency calculated for the inversed PSD shows an increase in both experiments compared to the measured value (an increase from 5.6 kHz to 11 kHz in 2018 and 10 to 19.1 kHz in 2021). The visual comparison shows that other than the power value, the main difference is the slope of the PSD at higher frequencies. In contrast, the PSD shape at lower frequencies has not been significantly affected. This shows that the inversion model corrects the attenuated signal at high frequencies, as explained in section 2.3 and Figure 1.

Figures 6c and 6d present (black line) the inversed power profile $\widehat{P_{s_m}}$ $(\mu Pa^2 \cdot m^{-2})$ which can be compared to the measured profile P_{p_n} (in red). The inversed power per unit area is one order of magnitude less than the measured power since each source contributes (by sound propagation and in a cumulative way) to each measured value. Moreover, the source spectrum was calculated for a distance of 1m from the source, while the measurements with the drift hydrophone were taken at a smaller distance (~ 30cm below the water surface <1m). The reconstructed integrated power profile $\widehat{P_{p_n}}$ (dashed lines) using the inversed signal, and Eq. 7, shows a good fit with the measured profile P_{p_n}.

To compare the measured and inversed power with the bedload flux profile, we scaled the signals by computing the ratio between the local value and the total cross-sectional value for each profile. Results are plotted in Figures 6e and 6f, which show a better synchronization of the bedload flux profile with the inversed power profile than the measured profile. This is particularly evident when considering the peaks and the sharp transition to low transport at the side of the section.

To numerically compare the profiles, the VEcv value is calculated for both the relative source and the relative measured profile in reference to the relative bedload flux profile. The Values of VEcv are presented in Figures 6e and 6f, confirming that the inversed source profile better illustrates the bedload flux in both experiments with less extent in the 2021 experiment than that for the 2018 experiment.
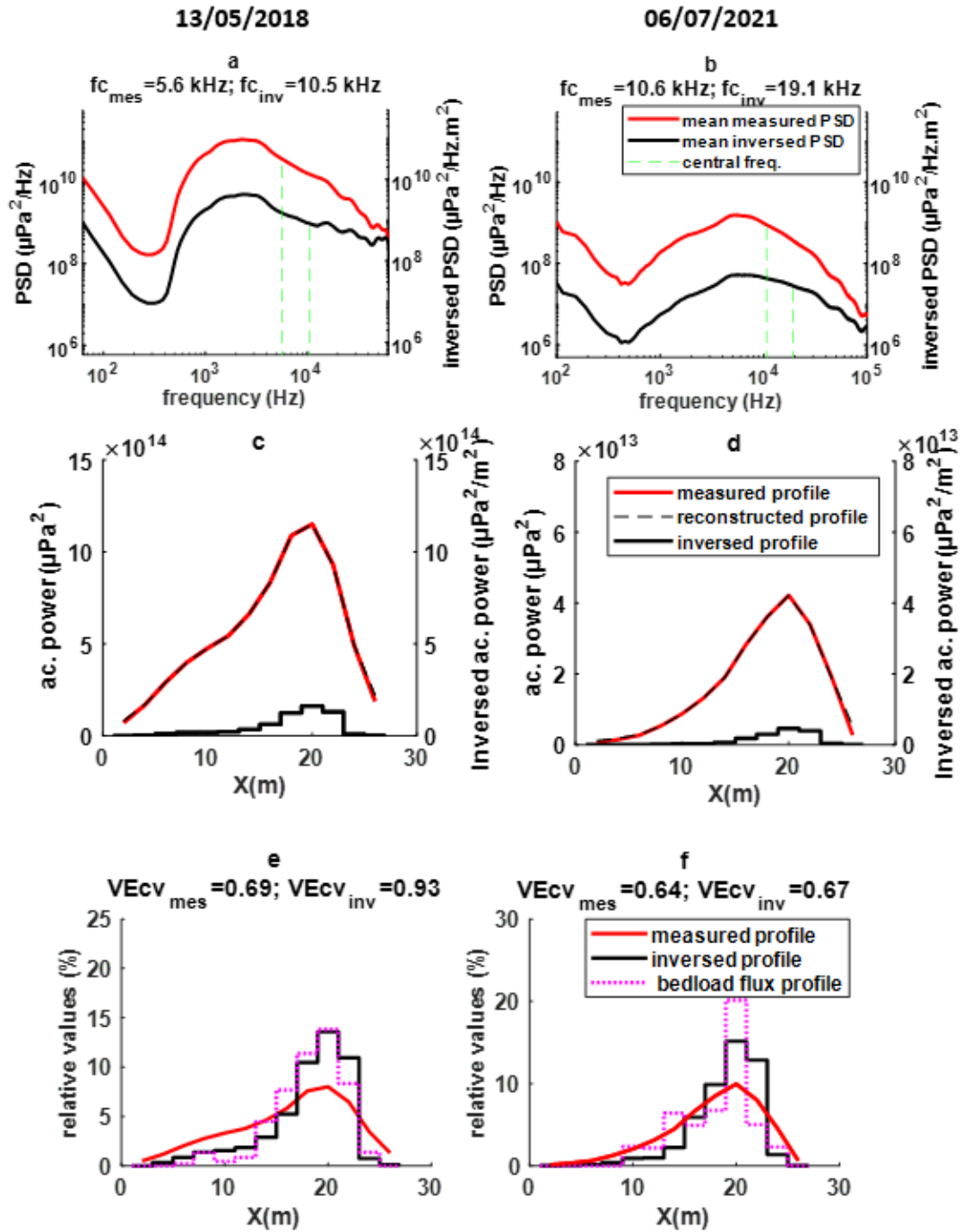
Figure 6 Mean measured PSD (in red) and inversed PSD (in black) for 2018 and 2021 in a) 2018 and b) 2021. Mean measured power (in red) and inversed power (in black) for c) 2018 and d) 2021 experiments. Relative profiles for e) 2018 and f) 2021, in magenta is the relative bedload flux profile

To study the effect of inversion on the acoustic power-bedload flux relation, the measured bedload flux value at each window n is plotted in figure 9 against the corresponding value of measured acoustic power (in black) and inversed acoustic power (in red) for both 2018 (circle) and 2021 (square) experiments. Depending on the experiment, we can differentiate two different trends for the measured acoustic power.

420 When the RMA reduced major axis regression (recommended when both X and Y data have uncertainties (Smith, 2009)) is applied to the measured data, the fitted power laws presented in the legend of Figure 9 shows two very distinct trends, with more than one order of magnitude of bedload flux for the same acoustic power values. On the other hand, the relationships obtained with the inversed data show a better continuation with less dispersion between the two experiments, allowing a unique fit with a good Pearson correlation coefficient (R^2=0.79).
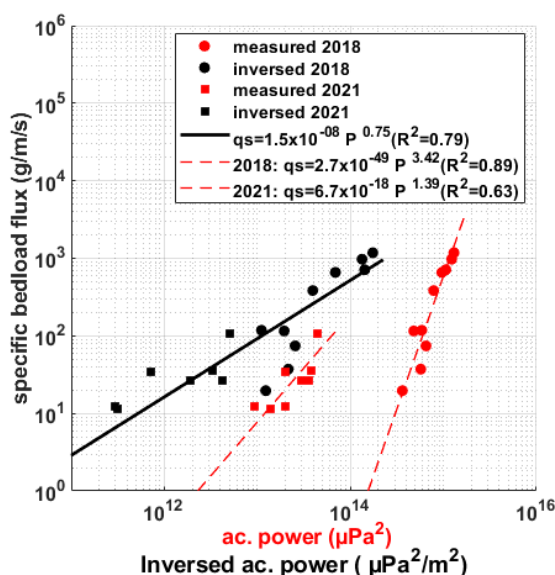
425

Figure 7 Local values of bedload flux vs local values of measured acoustic power (in black) and inversed acoustic power (in red)

6. Discussion

6.1 Dealing with uncertainties

The numerical testing in section 3.3 and Isere experiments have shown that extraneous noise sources might appear with different intensities due to uncertainty and perturbations in the measured acoustic profile. Meanwhile, the data collected on the

430 Giffre river shows variabilities in acoustic measurements as well as the bedload flux measurements (Figure 7). Thus, the inversion results of the Giffre application should consider the potential errors due to measuring variability. These uncertainties have been calculated by Geay et al. (2020), who estimated the relative uncertainty of acoustic measurements at 8% and 6%,

and the relative uncertainties associated to bedload flux at 29% and 32%, for 2018 and 2021 respectively. Several factors can contribute to the variability of bedload flux measurements, such as the efficiency of bedload samplers itself under different hydraulic conditions (Childers, 1999; Bunte et al., 2008). Moreover, the uncertainty of bedload sampling is also affected by the position of the sampler on the river bed (Vericat et al., 2006), where difficulties in controlling the exact position of the Elwha sampler were reported during our field measurements. Besides, in 2021 experiments, the number of bedload sampling repetitions was limited due to unstable flow conditions generated by a rainfall event after the beginning of the experiment. Then, the main difficulty in comparing inversed acoustic measurements with bedload flux profile is, in the first place, related to the quality of bedload flux sampling. Additional uncertainties also concern the attenuation coefficients obtained by fitting measurements of active test data showing variability up to a factor of 5 around the best fit.

6.2 Improvement of the calibration curve

The hydrophone measures not only its close environment but all sounds propagating in the river section. The cross-section integration results depend on the local condition, which can change with discharge, as shown in Figures 6c and 6d. This explains the two different qs=f(P) fits obtained for the Giffre river in Figure 7. In addition, the high power coefficients (2.4-3.5), much greater than unity aspredicted by the theory (Nasr et al), are also a consequence of the overestimation of the actual source energy. The global calibration curve of bedload flux obtained by Geay et al. (2020) is based on the average cross-sectional acoustic power values. The effects discussed here have probably contributed to part of the variability obtained when they fit their P(qs) function. More importantly, the global calibration curve may also generate an overestimation of bedload flux under certain conditions. For example, this calibration curve has been tested on the Drac River (a tributary of the Isere River), which is characterized by good sound propagation and a well-localized bedload channel. The result was an overestimation of the annual average bedload flux by a factor of more than 3.

On the other hand, Figure 7 shows that reducing these effects by inversing the acoustic power gives access to a better adjustment of the data obtained under different transport conditions. This offers a good potential for improving the global calibration curve proposed by Geay et al (2020), by adjusting a new function after inversing their whole data set. In this context, we used the inversion model on the dataset of Geay et al. (2020), which consists of 25 experiments of simultaneous bedload flux and acoustic measurements collected in 14 different rivers, covering a wide range of properties (e.g., slope, bedload intensity, and granulometry). The inversion model has been applied to all rivers, similarly to the Giffre river application. In the case of the absence of an active test on some rivers, a slope-based empirical formula (presented in supplementary material S2) from field data has been used to estimate the attenuation coefficient. The inversed and measured profiles for each river are presented in supplementary material Figures S1-S24.

Figure 8 shows the global calibration curve using the cross-sectional average measured acoustic power (in red) and the inversed calibration curve using the corresponding cross-sectional average inversed acoustic power (in black). Comparing both calibration curves shows that, when using inversed acoustic power, there is a minor decrease in variability (an increase of R^2 from 0.57 to 0.58), and a change of the fitted function with a lower power coefficient (decrease from 0.78 to 0.67). However,

the main difference between these two calibration curves to estimate bedload flux will require investigations with field measurements in particular in rivers with good sound propagation and localized bedload channel.
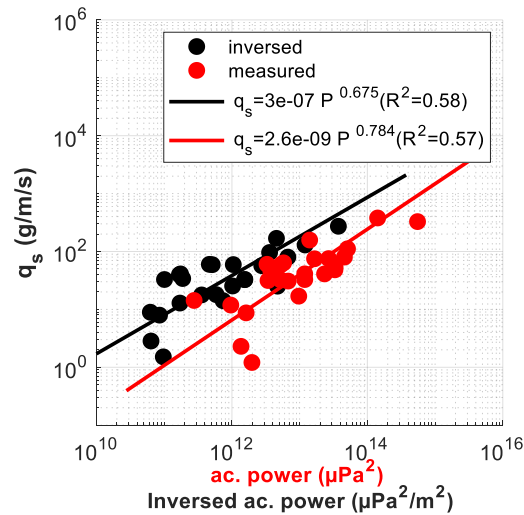
Figure 8 Comparison of global calibration curve fitted with cross-sectional average acoustic power (in red; Geay et al., 2020), and the readjusted curve fitted with cross-sectional average inversed acoustic power (in black)

6.3 Grain size detection

470 In lab experiments, the frequency content of the SGN has been well correlated with particle diameter (Thorne, 1985, 1986). However, in rivers, the attenuation SGN signal at high frequency is responsible in the first place for the underestimation of bedload GSD using acoustic measurements. The results in Figure 8 show a noticeable correction of the inversed PSD at high frequencies. To quantify the effect of inversion on bedload GSD estimation, the equivalent diameter D_{eq} is computed by the regress empirical formula of Thorne, (1985) between D_{eq} and central frequency:

475
$$f_c = \frac{209}{D_{eq}^{0.88}}, \quad (15)$$

Table 1 shows the computed D_{eq} compared to the measured D_{50} values. The most important observation is that the estimated diameters using SGN measurements overestimated the measured bedload diameter, as reported by (Geay et al., 2018). On the other hand, this overestimation is reduced when using the inversed source PSD. It is naïve to judge the inversion model and GSD estimation from the result of Eq. 15 as this experimental law has been carried out in controlled conditions using uniform

480 grain-size mixtures. However, results in Table 1 suggest a real improvement with the invesred signal. Additional effort can be made to GSD estimation by testing the model proposed by Petrut et al. (2018) for a bedload mixture using inversed signal; however, it is out of the scope of this article.

Table 1 Comparison of measured bedload D_{50} with estimated bedload equivalent diameter using measured and inversed PSD.

Experiment	2018	2021
Sampled D_{50} (mm)	6.8	3
D_{eq} from measured PSD (mm)	26.8	12.2
D_{eq} from inversed PSD (mm)	11.6	5.8

7. Conclusion

In this article, we present a new approach for the treatment of hydrophone measurements for bedload flux monitoring in rivers. This approach considers an inversion model for the measured acoustic profile of bedload self-generated noise SGN. The model seeks to locate the sources of SGN and calculates their power spectral density using a system of linear algebraic equations which combines acoustic measurements with acoustic signal transmission loss functions describing the propagation environment of the river.

Numerical testing show good performance of the model with variable degrees depending on the number of separated bedload active channels in the river cross-section and uncertainty in the measured acoustic profile. Field testing of the model on the Giffre river during two very different hydraulic conditions shows that the inversion model successively corrected the attenuation of the signal PSD. The signal correction by inversion compensates for lost of acoustic power due to the propagation mainly at high frequencies. Direct bedload measurements better correlate with inversed acoustic power profiles than measured acoustic power.

The methodology presented in this paper offers new perspectives for continuous bedload monitoring with hydrophones fixed on the river bank. Because they measure SGN for both near field and far-field, they are directly impacted by propagation effects, and ss a consequence, calibration is required. This calibration is possible with a reliable $qs(P)$ function associated with the drift measurement and acoustic inversion protocol.

Appendix A: Notations:

α	frequency-dependent attenuation coefficient	m^{-1}
a	attenuation factor	-
α_λ	dimensionless attenuation coefficient	-
$\alpha_{\lambda c}$	dimensionless attenuation coefficient for the cylindrical model	-
$\alpha_{\lambda s}$	dimensionless attenuation coefficient for the spherical model	-
$\mathcal{A}$	attenuation matrix	-
$\mathcal{A}^+$	pseudo-inverse of the matrix $\mathcal{A}$	-

$\mathcal{A}^-$	inverse of the matrix $\mathcal{A}$	-
$\mathcal{A}^t$	transpose of the matrix $\mathcal{A}$	-
c_f	celerity of sound in water	$m \cdot s^{-1}$
D	particle diameter	m
D_{eq}	bedload equivilant diamter	m
D_{50}	bedload median diamter	m
e	energy spectrum density	$\mu Pa^2 \cdot s \cdot Hz^{-1}$
ϵ	model error vector	-
f	frequency	Hz
fc	central frequency	Hz
f_{max}	maximum integration frequency	Hz
f_{min}	minimum integration frequency	Hz
i	bedload sample index	-
k	diameter class index	-
q_s	specific bedload flux	$g \cdot s^{-1} \cdot m^{-1}$
$\bar{q}_s$	average specific bedload flux	$g \cdot s^{-1} \cdot m^{-1}$
m	source index	-
M	number of sources	-
m	measurement index	-
N	number of measurements	-
n	measurement index	-
$P_{\mathcal{p}}$	integrated measured power	Pa^2
$\widehat{P_{\mathcal{p}_n}}$	integrated modeled measured power	Pa^2
$P_{\mathcal{s}}$	integrated source power	$Pa^2 \cdot m^{-2}$
$\widehat{P_{\mathcal{s}}}$	integrated inversed power	$Pa^2 \cdot m^{-2}$
$\overline{P_{\mathcal{s}}}$	average of all sources power in the river	$Pa^2 \cdot m^{-2}$
$\mathcal{p}$	measured PSD	$\mu Pa^2 \cdot Hz^{-1}$
$\mathcal{P}$	measured PSD vector	$Pa^2 \cdot Hz^{-1}$
$\widehat{\mathcal{P}}$	modeled PSD vector	$Pa^2 \cdot Hz^{-1}$
r	distance source-hydrophone	m
s	PSD for a point source	$Pa^2 \cdot Hz^{-1}$
$\mathcal{s}$	source PSD per unit area	$Pa^2 \cdot Hz^{-1} \cdot m^{-2}$
$\widehat{\mathcal{s}_m}$	inveresed PSD per unit area	$Pa^2 \cdot Hz^{-1} \cdot m^{-2}$
$\mathcal{S}$	sources PSD vector	$Pa^2 \cdot Hz^{-1} \cdot m^{-2}$

Earth **Surface**
Dynamics
Discussions

$\widehat{s}$	inversed PSD vector	$Pa^2 \cdot Hz^{-1} \cdot m^{-2}$
σ	condition number	-
TL	transmission loss function	-
TL_1	geometrical spreading function	-
TL_2	scattering and absorption function	-
$VEcv$	variance-explained accuracy measure	-
W	width of the river	m
W_M	width of the sources	m
x_{hyd}	hydrophone x coordinate	m
y_{hyd}	hydrophone y coordinate	m
z_{hyd}	hydrophone x coordinate	m

Data availability

Data supporting this article are uploaded to (Nasr, Mohamad; Johannot, Adele ; Geay, Thomas ; Zanker, Sebastien ; Recking, Alain; Le Guern, Jules (2022), "Optimization of passive acoustic bedload monitoring in rivers by signal inversion ", Mendeley
505 Data, V1, doi: 10.17632/vygy6tsy5n.1). Additional supplementary material document that supports the results presented in section 6.3 of the manuscript is uploaded to the journal.

References

Akay, A., Hodgson, T. H., Akay, A., and Hodgson, T. H.: Sound radiation from an accelerated or decelerated sphere, 63, 313–318, https://doi.org/10.1121/1.381740, 1978.

510 Arthur, F., Christophe, P., Thibaut, L. E. M., Quentin, L., Ea, L. V. A., and Antonio, P.: Microphone array techniques based on matrix inversion, in: VKI Lecture Series STO-AVT- 287, Lecture Series von Karman institute for Fluid Dynamics 2017, 1–24, 2017.

Auel, C., Albayrak, I., Sumi, T., and Boes, R. M.: Sediment transport in high-speed flows over a fixed bed: 2. Particle impacts and abrasion prediction, Earth Surf. Process. Landforms, 42, 1384–1396, https://doi.org/10.1002/esp.4132, 2017.

515 Bakker, M., Gimbert, F., Geay, T., Misset, C., Zanker, S., and Recking, A.: Field Application and Validation of a Seismic Bedload Transport Model, J. Geophys. Res. Earth Surf., 125, e2019JF005416, https://doi.org/10.1029/2019JF005416, 2020.

Barton, J., Slingerland, R. R. L., Pittman, S., and Gabrielson, T. B.: Monitoring coarse bedload transport with passive acoustic instrumentation: A field study, US Geol. Surv. Sci. Investig. Rep., 38–51, 2010.

Bunte, K., Abt, S. R., Potyondy, J. P., and Swingle, K. W.: A Comparison of Coarse Bedload Transport Measured with Bedload
520 Traps and Helley-Smith Samplers, Geodin. Acta, 21, 53–66, https://doi.org/10.3166/ga.21.53-66, 2008.

Earth Surface
Dynamics
Discussions

Childers, D.: Field comparisons of six pressure-difference bedload samplers in high-energy flow, Water-Resources Investig. Rep., 1999.

Claude, N., Rodrigues, S., Bustillo, V., Bréhéret, J. G., Macaire, J. J., and Jugé, P.: Estimating bedload transport in a large sand–gravel bed river from direct sampling, dune tracking and empirical formulas, 179, 40–57, https://doi.org/10.1016/J.GEOMORPH.2012.07.030, 2012.

Edwards, T. K. and Glysson, G, D.: WSGS science for a changing world Field Methods for Measurement of Fluvial Sediment. InTechniques ofWater-Resources Investigations United States Geological Survey Report, 89 pp., 1999.

Ergenzinger, P., de Jong, C., Laronne, J., and Reid, I.: Short term temporal variations in bedload transport rates: Squaw Creek, Montana, USA and Nahal Yatir and Nahal Estemoa, Israel, 251–264, https://doi.org/10.1007/BFB0117844, 1994.

Etter, P. C.: Underwater acoustic modeling and simulation, fifth edition, CRC Press, Fifth edition. | Boca Raton : CRC Press, Taylor & Francis Group, 1–608 pp., https://doi.org/10.1201/9781315166346, 2018.

Ferguson, R. I., Parsons, D. R., Lane, S. N., and Hardy, R. J.: Flow in meander bends with recirculation at the inner bank, Water Resour. Res., 39, 1322, https://doi.org/10.1029/2003WR001965, 2003.

Field, R. L., Jarosz, E., and Moum, J. N.: Acoustic Propagation in Turbulent Layers, in: OCEANS 2007, 1–7, https://doi.org/10.1109/OCEANS.2007.4449152, 2007.

Geay, T.: Mesure acoustique passive du transport par charriage dans les rivières [Passive Acoustic measurement of bedload transport in rivers], 2013.

Geay, T., Belleudy, P., Laronne, J. B., Camenen, B., and Gervaise, C.: Spectral variations of underwater river sounds, Earth Surf. Process. Landforms, 42, 2447–2456, https://doi.org/10.1002/esp.4208, 2017.

Geay, T., Zanker, S., Petrut, T., and Recking, A.: Measuring bedload grain-size distributions with passive acoustic measurements, E3S Web Conf., 40, 04010, https://doi.org/10.1051/e3sconf/20184004010, 2018.

Geay, T., Michel, L., Zanker, S., and Rigby, J. R.: Acoustic wave propagation in rivers: an experimental study, Earth Surf. Dyn., 7, 537–548, https://doi.org/10.5194/esurf-7-537-2019, 2019.

Geay, T., Zanker, S., Misset, C., and Recking, A.: Passive Acoustic Measurement of Bedload Transport: Toward a Global Calibration Curve?, J. Geophys. Res. Earth Surf., 125, e2019JF005242, https://doi.org/10.1029/2019JF005242, 2020.

Gimbert, F., Fuller, B. M., Lamb, M. P., Tsai, V. C., and Johnson, J. P. L.: Particle transport mechanics and induced seismic noise in steep flume experiments with accelerometer-embedded tracers, Earth Surf. Process. Landforms, 44, 219–241, https://doi.org/10.1002/esp.4495, 2019.

Golub, G. H. (Gene H. and Van Loan, C. F.: Matrix computations, 694, 1996.

Gray, J. R., Laronne, J. B., and Marr, J. D. G.: Bedload-Surrogate Monitoring Technologies Scientific Investigations Report 2010 – 5091, U.S.Geological Survey, 37 pp., 2010.

Hamilton, E.: Acoustic properties of sediments, 1987.

Jensen, F. B., Kuperman, W. A., Porter, M. B., and Schmidt, H.: Fundamentals of Ocean Acoustics, Comput. Ocean Acoust., 1–64, https://doi.org/10.1007/978-1-4419-8678-8_1, 2011.

555 Johnson, P. and Muir, T. C.: Acoustic Detection Of Sediment Movement, J. Hydraul. Res., 7, 519–540, https://doi.org/10.1080/00221686909500283, 1969.

Koss, L. L. and Alfredson, R. J.: Transient sound radiated by spheres undergoing an elastic collision, J. Sound Vib., 27, 59–75, https://doi.org/10.1016/0022-460X(73)90035-7, 1973.

Koss, L. L., Koss, and L., L.: Transient sound from colliding spheres—Inelastic collisions, 36, 555–562,
560 https://doi.org/10.1016/S0022-460X(74)80121-5, 1974.

Lamb, M. P., Dietrich, W. E., and Venditti, J. G.: Is the critical Shields stress for incipient sediment motion dependent on channel-bed slope?, J. Geophys. Res., 113, F02008, https://doi.org/10.1029/2007JF000831, 2008.

Li, J.: Assessing the accuracy of predictive models for numerical data: Not r nor r2, why not? Then what?, PLoS One, 12, https://doi.org/10.1371/JOURNAL.PONE.0183250, 2017.

565 Madoliat, R., Nouri, N. M., and Rahrovi, A.: Developing general acoustic model for noise sources and parameters estimation, AIP Adv., 7, 025014, https://doi.org/10.1063/1.4977185, 2017.

Mao, L., Carrillo, R., Escauriaza, C., and Iroume, A.: Flume and field-based calibration of surrogate sensors for monitoring bedload transport, 253, 10–21, https://doi.org/10.1016/j.geomorph.2015.10.002, 2016.

Nasr, M., Geay, T., Zanker, S., and Recking, A.: A Physical Model for Acoustic Noise Generated by Bedload Transport in
570 Rivers, J. Geophys. Res. Earth Surf., 127, https://doi.org/10.1029/2021JF006167, 2021.

Nelson, P. A. and Yoon, S. H.: ESTIMATION OF ACOUSTIC SOURCE STRENGTH BY INVERSE METHODS: PART I, CONDITIONING OF THE INVERSE PROBLEM, J. Sound Vib., 233, 639–664, https://doi.org/10.1006/JSVI.1999.2837, 2000.

Pekeris, C. L.: Theory of propagation of explosive sound in shallow water, Mem. Geol. Soc. Am., 27, 1–116,
575 https://doi.org/10.1130/MEM27-2-p1, 1948.

Petrut, T., Geay, T., Gervaise, C., Belleudy, P., and Zanker, S.: Passive acoustic measurement of bedload grain size distribution using self-generated noise, Hydrol. Earth Syst. Sci., 22, 767–787, https://doi.org/10.5194/hess-22-767-2018, 2018.

Presezniak, F. and Guillaume, P.: Aeroacoustic source identification using a weighted pseudo inverse method, 16th AIAA/CEAS Aeroacoustics Conf. (31st AIAA Aeroacoustics Conf., https://doi.org/10.2514/6.2010-3725, 2010.

580 Recking, A.: An analysis of nonlinearity effects on bed load transport prediction, J. Geophys. Res. Earth Surf., 118, 1264–1281, https://doi.org/10.1002/jgrf.20090, 2013.

Rickenmann, D., Turowski, J. M., Fritschi, B., Wyss, C., Laronne, J., Barzilai, R., Reid, I., Kreisler, A., Aigner, J., Seitz, H., and Habersack, H.: Bedload transport measurements with impact plate geophones: comparison of sensor calibration in different gravel-bed streams, Earth Surf. Process. Landforms, 39, 928–942, https://doi.org/10.1002/esp.3499, 2014.

585 Rigby, J. R., Wren, D. G., and Kuhnle, R. A.: Passive Acoustic Monitoring of Bed Load for Fluvial Applications, J. Hydraul. Eng., 142, 02516003, https://doi.org/10.1061/(ASCE)HY.1943-7900.0001122, 2016.

Roh, H.-S., Sutin, A., and Bunin, B.: Determination of acoustic attenuation in the Hudson River Estuary by means of ship noise observations, J. Acoust. Soc. Am., 123, EL139–EL143, https://doi.org/10.1121/1.2908404, 2008.

Smith, R. J.: Use and misuse of the reduced major axis for line-fitting, Am. J. Phys. Anthropol., 140, 476–486,
590 https://doi.org/10.1002/AJPA.21090, 2009.

Thorne, P. D.: The measurement of acoustic noise generated by moving artificial sediments, J. Acoust. Soc. Am., 78, 1013–
1023, https://doi.org/10.1121/1.393018, 1985.

Thorne, P. D.: Laboratory and marine measurements on the acoustic detection of sediment transport, J. Acoust. Soc. Am., 80,
899–910, https://doi.org/10.1121/1.393913, 1986.

595 Thorne, P. D.: Seabed generation of ambient noise, J. Acoust. Soc. Am., 87, 149–153, https://doi.org/10.1121/1.399307, 1990.

Thorne, P. D.: An overview of underwater sound generated by interparticle collisions and its application to the measurements
of coarse sediment bedload transport, Earth Surf. Dyn., 2, 531–543, https://doi.org/10.5194/esurf-2-531-2014, 2014.

Thorne, P. D. and Foden, D. J.: Generation of underwater sound by colliding spheres, J. Acoust. Soc. Am., 84, 2144–2152,
https://doi.org/10.1121/1.397060, 1988.

600 Vér, I. L. (István L. . and Beranek, L. L. (Leo L.: Noise and vibration control engineering : principles and applications, Wiley,
966 pp., 2007.

Vericat, D., Church, M., and Batalla, R. J.: Bed load bias: Comparison of measurements obtained using two (76 and 152 mm)
Helley-Smith samplers in a gravel bed river, Water Resour. Res., 42, https://doi.org/10.1029/2005WR004025, 2006.

Whiting, P. J. and Dietrich, W. E.: Boundary Shear Stress and Roughness Over Mobile Alluvial Beds, J. Hydraul. Eng., 116,
605 1495–1511, https://doi.org/10.1061/(ASCE)0733-9429(1990)116:12(1495), 1990.

Wolman, M. G.: A method of sampling coarse riverbed material, Trans. Am. Geophys. Union, 35, 951,
https://doi.org/10.1029/TR035i006p00951, 1954.

Wren, D. G., Goodwiller, B. T., Rigby, J. R., Carpenter, W. O., Kuhnle, R. A., and Chambers, J. P.: Sediment-Generated Noise
(SGN): laboratory determination of measurement volume, in: Proc. 3rd Jt. Fed. Interag. Conf. (10th Fed. Interag. Sediment.
610 Conf. 5th Fed. Interag. Hydrol. Model. Conf. April 19 – 23, 2015, Reno, Nevada., 408–413, 2015.